DOI: 10.15480/882.9333

Eighth International Symposium on Marine Propulsors
smp'24, Berlin, Germany, March 2024

Influence of leeway on hull-propeller-rudder interaction using CFD methods*

Yifu Zhang[1,2], Saeed Hosseinzadeh[1], Joseph Banks[1], Dominic Hudson[1], Stephen Turnock[1]

[1]Maritime Engineering Research Group, School of Engineering, University of Southampton, UK
[2]High Performance Computing (HPC) Team, iSolutions, University of Southampton, UK

ABSTRACT

Due to the decarbonization challenges within the maritime sector, there is an increased focus on improving vessel propulsive energy efficiency. Wind-assisted propulsion is able to reduce emissions through retrofit systems that generate thrust from the wind. Wind-assisted vessels are subjected to increased aerodynamic forces and develop an inherent leeway and rudder angle to compensate for the lateral forces and yaw moments. Therefore, a good understanding of the impact of leeway on a ship's propulsive efficiency is vital for the design and operation of wind-assisted ships. This also contributes to a better insight into the physics of hydrodynamic interaction between the hull, propeller, and rudder while manoeuvring in seaways. In this paper, the KRISO Container Ship (KCS) model scale is chosen for numerical computations under three different leeway angles ($-10°$, $0°$, $+10°$) with a series of rudder angles. It is found that KCS's drag and lateral forces increase with the increment of rudder angle in non-zero leeway conditions, and the rotating propeller intensifies this increasing trend. Rudder forces are mainly dependent on the upstream propeller performance and higher propeller loading tends to shift the rudder lift.

Keywords

Wind assisted shipping, leeway angle, hull-propeller-rudder interaction, Computational Fluid Dynamics (CFD).

1 INTRODUCTION

With an increased focus on improving ship propulsive energy efficiency and achieving the goal of decarbonization within maritime sectors, it is necessary to gain a better understanding of ships' hydrodynamic performance in real sea states (Molland et al. 2017), which is closely related to ship manoeuvring in waves. Although the experimental approach, such as the free-running model and captive model tests in a towing tank or wave basin, can provide accurate predictions of ship manoeuvrability, this conventional method is still very costly and has a high specification for test models and facilities. With the rapid development of high performance computing technologies, the numerical method using Computational Fluid Dynamics (CFD) is a highly promising and cost-effective alternative, and it can accurately resolve the local flow characteristic around the hull and its appendages, which is less likely to be captured in towing tank experiments.

In assessing a ship's manoeuvring and power in real seaways, accurately estimating the forces and moments on the hull and appendages is crucial. This is particularly vital at the leeway angle, where the rudder and leeway angles greatly impact the ship's resistance and propulsion efficiency. Sanada et al. (2021) used both experimental methods and CFD to investigate the dynamics of the KCS hull-appendage interaction during turning manoeuvres and explained the reason for differences between port and starboard turning. Meyer et al. (2022) analyzed the interaction between the JBC hull and propeller in both positive and negative static drift scenarios, presenting in-depth findings on the fore-body vortex characteristics. Besides, with the increasing demand for ships compliant with IMO standards, wind-assist propulsion devices are becoming a popular eco-friendly option. Unlike conventional ships, wind-assisted vessels often navigate at a leeway angle, using the rudder to counteract significant side forces and yaw moments. Hence, understanding the impact of leeway on ship powering is crucial for evaluating their navigation and manoeuvring capabilities and guiding the design and operation of future wind-assisted vessels.

This paper investigates the effect of leeway on the hull-propeller-rudder interaction of the benchmark KCS in calm water using CFD. Simulations of the fully appended KCS at different leeway angles, combined with different rudder angles, are performed. This method significantly cuts computational expenses and offers valuable insights for experimental force measurements on the hull and appendages under leeway conditions.

2 NUMERICAL METHODOLOGY

2.1 Governing equations

The Reynolds Averaged Navier-Stokes (RANS) equations are used to model the fluid flow around the KCS in leeway conditions. With the assumption of an incompressible fluid, the set of equations can be written as:

$$\frac{\partial \overline{u}_i}{\partial x_i} = 0 \tag{1}$$

$$\rho \frac{\partial \overline{u}_i}{\partial t} + \rho \frac{\partial \overline{u}_i \overline{u}_j}{\partial x_j} = - \frac{\partial \overline{p}}{\partial x_i} + \frac{\partial}{\partial x_j} \left[\mu \left(\frac{\partial \overline{u}_i}{\partial x_j} + \frac{\partial \overline{u}_j}{\partial x_i} \right) \right] - \rho \frac{\partial \overline{u_i' u_j'}}{\partial x_j} + \overline{F_i} \tag{2}$$

where $\overline{u}$ and $\overline{p}$ are the mean velocity and pressure fields, $\overline{F_i}$ is the body force term, ρ is the fluid density, and μ is the dynamic viscosity. The Reynolds stress $\overline{u_i' u_j'}$ is modelled using the Shear Stress Transport (SST) $k-\omega$ turbulence model to achieve turbulence closure. The SST $k-\omega$ model has been successfully adopted for analyzing hull-propeller-rudder interaction (Larsson et al. 2013) and computing manoeuvring hydrodynamic forces in drift motion (Phillips et al. 2009).

2.2 RANS solver

The governing equations are numerically solved using the open-source RANS solver OpenFOAM version 7 and RANS equations are discretised using the Finite Volume Method (FVM). The OpenFOAM interFoam solver is adopted, tailored for simulating interactions between two non-mixing, incompressible fluids like water and air in two-phase flows. This solver employs the PIMPLE algorithm for pressure-velocity coupling, a hybrid of PISO and SIMPLE algorithms. PIMPLE incorporates velocity correction and under-relaxation, enhancing its suitability for transient flow modelling. This is particularly effective in modelling ship stern flows, where unsteady fluid dynamics are significant. The Volume of Fluid (VOF) technique is utilized to capture the impact of a free surface and to depict the dynamic interactions at the boundary between water and air.

2.3 Propeller modelling

This study focuses on the interaction between the hull, propeller, and rudder in leeway conditions, with less emphasis on detailed propeller analysis. To this end, two body force models, the Blade Element Momentum Theory (BEMt) and the Yamazaki model, are adopted for propeller evaluation. These models offer an advantage over fully discretized propellers by removing the need to create complex meshes for rotating domains and detailed propeller blades. This simplification not only greatly cuts down on computational costs but also eases the handling of geometric complexities, especially for propellers in or near stationary flow conditions. In body force approaches, the momentum from the propeller blades' rotation is incorporated directly into the RANS momentum equation as an additional momentum source, therefore simplifying the overall analysis.

The Blade Element Momentum Theory (BEMt), initially introduced by Burrill (1944), effectively merges axial momentum theory with the two-dimensional blade element theory. It calculates lift and drag based on the airfoil's angle of attack, which depends on the local pitch, incoming velocity incidence, propeller rotation, and nominal wake characteristics. The integration of blade element theory into momentum theory involves aligning their efficiency calculations. BEMt requires pre-existing data on blade section lift and drag characteristics. The lift coefficient (C_L) is calculated from the thrust force balance in the previous iteration, while the drag coefficient (C_D) is obtained from a fitted curve to experimental $C_D - \alpha$ data. This study follows the BEMt methodology outlined by Molland et al. (2017). The coupling of RANS and BEMt has been effective in assessing ship hydrodynamics and the interaction between the hull, propeller, and rudder, as demonstrated by Zhang (2023). Additionally, BEMt has been validated as an accurate and cost-efficient method for RANS predictions of static drift and manoeuvring in self-propelled ships (Turnock et al. 2008).

The Yamazaki model, a blend of lifting line and lifting surface approaches, was initially conceptualized by Yamazaki (1968) and further refined by Moriyama (1979) and Yamazaki (1998). This model simulates the propeller's function by allocating bound vortices instead of actual blades, and it employs a pitched free vortex to represent the trailing wake. The vortex strength is methodically distributed over a concentric grid centred around the propeller's centroid. For a comprehensive explanation of this method, refer to the detailed accounts provided by Winden (2021a, 2021b).

3 CASE DESCRIPTION

3.1 Hull geometry

Due to comprehensive previous research involving both experimental and computational studies, the KCS model, with a scale ratio of $\lambda = 31.60$ (where $L_{PP} = 7.2786m$), is selected as the subject vessel in all simulation cases of this study. This particular model aligns with the KCS model 1 from the 2015 Tokyo CFD workshop, as detailed by Hino et al. (2020). The geometry of the KCS hull and rudder from the side view is shown in Figure 1. The primary specifications of KCS for both full-scale and model-scale are listed in Table 1.

Table 1: Main Particulars of KCS

Parameter	Full Scale	Model Scale
Scale ratio, λ	1	31.60
Length, L_{pp}	230 m	7.2786 m
Depth, D	19 m	0.6013 m
Draft, T	10.8 m	0.3418 m
Displacement, ∇	52030 m^3	1.6490 m^3
Wetted surface area, S_W	9424 m^2	9.4379 m^2
Froude Number, Fn	0.26	0.26
Design speed, U	12.35 m/s	2.196 m/s
Propeller diameter, D_P	7.9 m	0.25 m
Propeller hub ratio, D_H/D_P	0.18	0.18
Propeller blades, Z	5	5

Figure 1: The geometry of the KCS hull and rudder

3.2 Coordinate systems

In simulating a ship under leeway, two coordinate systems are used: the computational domain and the ship-fixed system. The ship-fixed system, aligning with the right-hand rule, includes an x-axis towards the bow, a y-axis to starboard, and an origin at mid-ship. The leeway angle β is positive when veering starboard, while the rudder angle β_r is positive when turned starboard. Hydrodynamic forces and moments are mainly calculated in the ship-fixed system. The ship's resistance (R), lateral force (F_Y), and yaw moment (M_Z), along with rudder drag (D) and lift (L), are measured in this system, as shown in Figure 2.

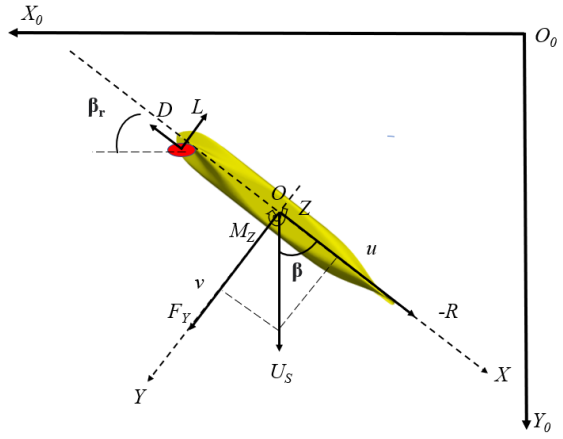

Figure 2: Coordinate systems and variables from bottom

3.3 Simulation conditions

Three sets of simulations are carried out on the KCS hull with the rudder. Three leeway angles are selected: β= -10°, β= 0°, β= +10°. For each, an array of static rudder angles is tested. Initially, a calm water resistance test is conducted for all scenarios. Following this, three fixed RPM tests are carried out, with RPMs set at 600, 900, and 1200. Both the BEMt and Yamazaki model are employed to capture the influence of the propeller. Detailed descriptions of these simulation conditions are provided below.

- Leeway angle, β= 0°, with eleven static rudder angles, β_r= -35°, -30°, -20°, -10°, -5°, 0°, 5°, 10°, 20°, 30°, 35°.
- Leeway angle, β= -10°, with seven static rudder angles, β_r= -20°, -10°, -5°, 0°, 5°, 10°, 20°.
- Leeway angle, β= +10°, with seven static rudder angles, β_r= -20°, -10°, -5°, 0°, 5°, 10°, 20°.

3.4 Computational domain and boundary conditions

The numerical simulation domain for the KCS hull with a rudder is designed in compliance with the CFD application standards provided by the ITTC (2014). The inlet boundary of the simulation is located $1.0L_{pp}$ ahead of the KCS fore perpendicular (FP), while the outlet boundary is $3.0L_{pp}$ behind the KCS aft perpendicular (AP). To reduce the influence of the walls on the simulation, the side boundaries are set $1.5L_{pp}$ away from the KCS hull's mid-ship. The bottom boundary is placed $1.5L_{pp}$ beneath the free surface, and the top boundary is $1.0L_{pp}$ above the free surface. Figure 3 depicts the configuration of the computational domain, from both side and top views.

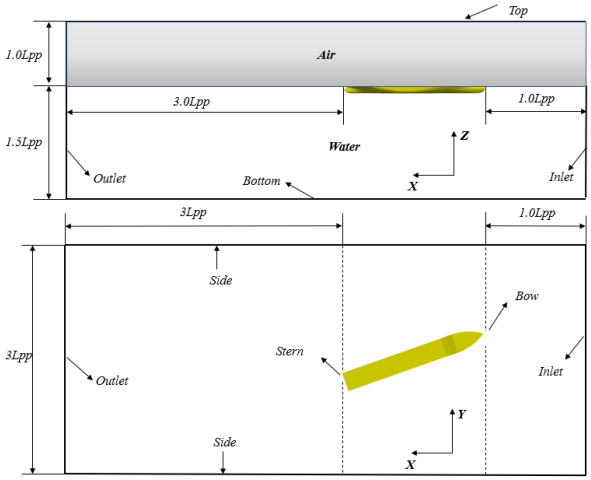

Figure 3: Computational domain arrangement

The inlet boundary conditions employ a fixed velocity and a zero pressure gradient. The hull and rudder utilize a non-slip condition for velocity and a zero normal gradient for pressure. At the outlet, both velocity and pressure are subject to a zero gradient condition. For the top, sides, and bottom of the domain, a slip boundary condition is applied.

4 MESH GENERATION

The grid for simulating the KCS hull and rudder is generated using OpenFOAM's blockMesh and snappyHexMesh utilities. Initially, blockMesh creates a hexahedral structured mesh for the computational domain, refining it especially around the free surface. Four refinement boxes are then used to improve mesh resolution near the KCS hull and rudder, with cells divided horizontally and vertically. To ensure a smooth mesh density transition, refinement zones are gradually reduced at each level. Additionally, a smaller box further refines the mesh around the stern, encompassing the hull's aft, the rudder, and the propeller area. For accurate boundary layer representation, the first cell height is set to achieve a $y^+ = 1$ target. Finally, snappyHexMesh adds eight prism layers to the hull and rudder surfaces, expanding at a 1.2 ratio as per ITTC recommendations. Figure 4 offers a detailed side view of the grid layout around the KCS at 0° leeway with zero degree rudder angle. Table 2 presents the average y^+ values for each component and the total mesh sizes across three leeway scenarios. These figures are derived from the KCS model with a zero-degree rudder angle. It should be noted that while values might slightly differ in scenarios with non-zero rudder angles, these variations are typically minor.

Table 2: Average y^+ and total mesh size for different leeway cases (with free surface)

Parameter	$\beta = -10°$	$\beta = 0°$	$\beta = +10°$
y^+ of hull	1.13	1.05	1.13
y^+ of rudder blade	0.33	0.42	0.34
y^+ of rudder skeg	0.40	0.59	0.39
Total mesh size	15.37M	16.25M	15.32M

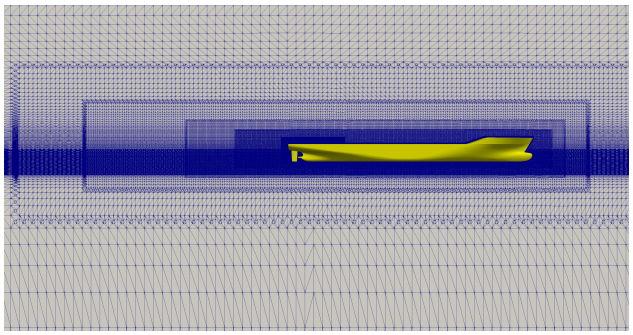

Figure 4: Grid distribution from side view for 0°leeway KCS with 0°rudder angle including free surface.

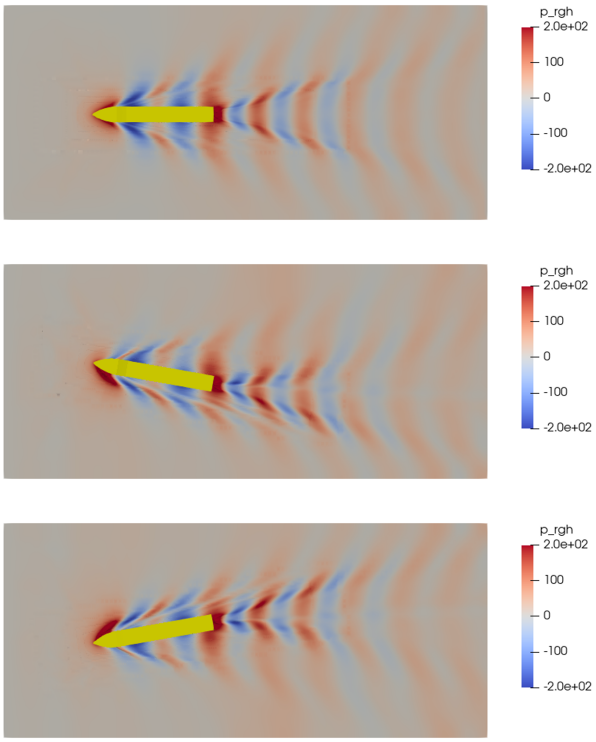

Figure 5: Hydrodynamic pressure distribution on the free surface with different leeway angles in resistance tests, Fn=0.26. β=0°, β_r=0°(top); β=+10°, β_r=0°(middle); β=-10°, β_r=0°(bottom).

In addition, hydrodynamic pressure distribution on the free surface at three static leeway angles is presented in Figure 5, demonstrating a good resolution using the selected mesh density.

5 RESULTS

5.1 Hull-rudder interaction under leeway

Figure 6 illustrates how leeway and rudder angle impact the total resistance coefficient, C_T, which represents the combined drag from the hull and rudder, expressed non-dimensionally. It is observed that drag force rises with an increase in rudder angle under conditions where the vessel is moving straight ahead; the C_T curve is almost symmetrical around the β_r=0° line. Introducing a leeway angle causes an upward shift in the drag force curves at β = -10° and +10°, with the peak C_T value occurring at a +20° rudder angle for positive leeway angles and at -20° for negative leeway angles. Figure 7 shows the influence of leeway angle on lateral force experienced by KCS. Regarding the non-dimensional lateral force $F_Y^{'}$ under straight-ahead motion, it tends to grow as the rudder angle's absolute value increases, with the direction of the side force matching the rudder angle's sign. When there is leeway, the slope of the lateral force curve remains relatively unchanged, yet positive and negative leeway angles result in respective upward and downward shifts. The leeway angle's effect on lateral force is more pronounced than that of the rudder angle.

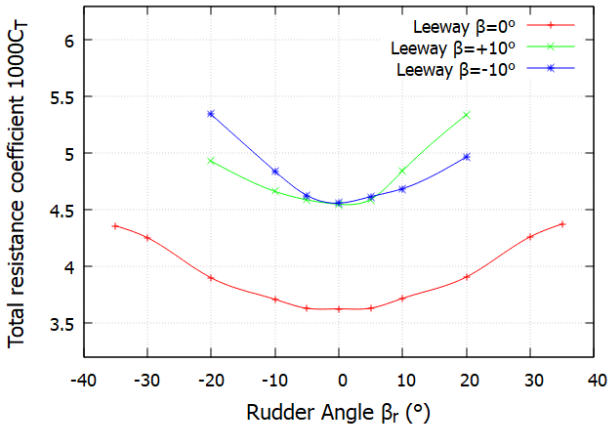

Figure 6: Effect of leeway on KCS drag force.

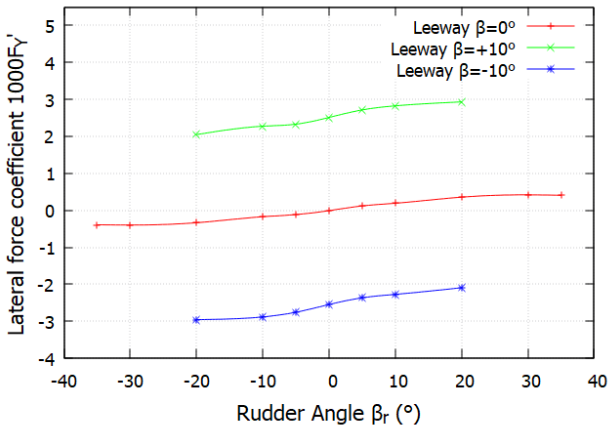

Figure 7: Effect of leeway on KCS lateral force.

Figures 8 and 9 depict how rudder forces are affected by static leeway and the angle of the rudder. With a larger angle of attack, an increase in rudder angle results in heightened rudder force. The presence of a leeway angle intensifies the steepness of the rudder drag curve compared to scenarios with no leeway. Moreover, introducing leeway angles causes a vertical displacement in the rudder lift curve, though the effect on the curve's steepness remains comparatively slight.

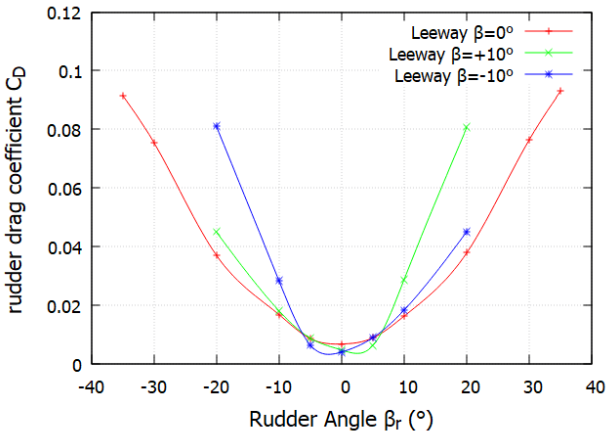

Figure 8: Effect of leeway on KCS rudder drag.

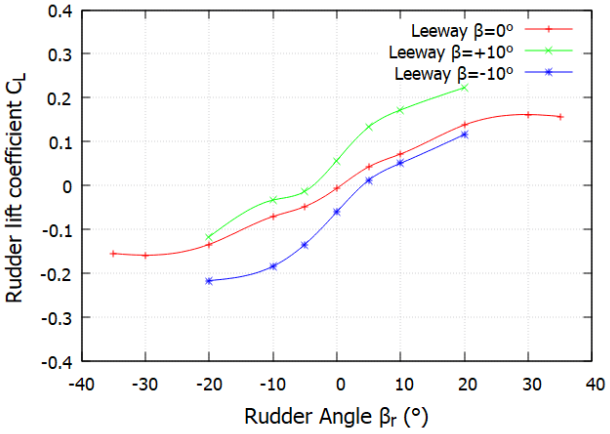

Figure 9: Effect of leeway on KCS rudder lift

5.2 Hull-propeller-rudder interaction under leeway

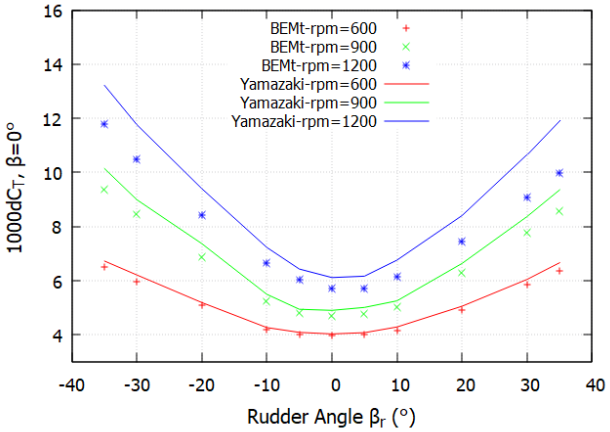

Figure 10: Zero leeway KCS's C_T predicted by BEMt and Yamazaki under different RPMs' conditions

Figure 10 presents the computed total resistance coefficients (C_T) of the KCS in zero leeway for various propeller revolution speeds using both the BEMt and Yamazaki models. Two models consistently show that the KCS total resistance coefficients (C_T) increase as the rudder angle becomes larger, indicating a rise in overall drag. Additionally, an increase in propeller revolution speed results in greater total drag, which can be attributed to lower pressure at the back of the hull. The single-direction rotation of the propeller causes more drag at a negative rudder angle than at a corresponding positive angle. The results of BEMt and Yamazaki models generally concur, but their differences are more pronounced at higher propeller speeds.

Tables 3 and 4 present the KCS total resistance coefficients (C_T) under non-zero leeway conditions (β = -10°, +10°). To evaluate the rudder's impact on the KCS total resistance under leeway, a comparison is conducted of the C_T value differences (dC_T) between non-zero leeway and zero leeway conditions, as depicted in Figure 11. It is observed that the applied leeway angle notably increases the total resistance, exhibiting divergent trends for positive and negative leeways: For a +10° leeway angle, dC_T escalates as the rudder angle shifts from -20° to +20°, whereas for a -10° leeway angle, the dC_T trend diminishes with changing rudder angles.

Table 3: Total drag coefficient at leeway angles +10°and -10°, predicted by BEMt under different RPMs

Leeway	Rudder	rpm=600	rpm=900	rpm=1200
+10°	-20°	5.394	6.916	8.517
+10°	-10°	4.861	5.600	6.902
+10°	-5°	4.701	5.347	6.389
+10°	0°	4.659	5.278	6.224
+10°	5°	4.728	5.394	6.458
+10°	10°	4.929	5.749	7.078
+10°	20°	5.956	7.468	8.704
-10°	-20°	6.403	8.143	9.702
-10°	-10°	5.367	6.415	7.606
-10°	-5°	4.872	5.762	6.827
-10°	0°	4.623	5.413	6.356
-10°	5°	4.636	5.185	6.245
-10°	10°	4.816	5.366	6.433
-10°	20°	5.411	6.314	7.519

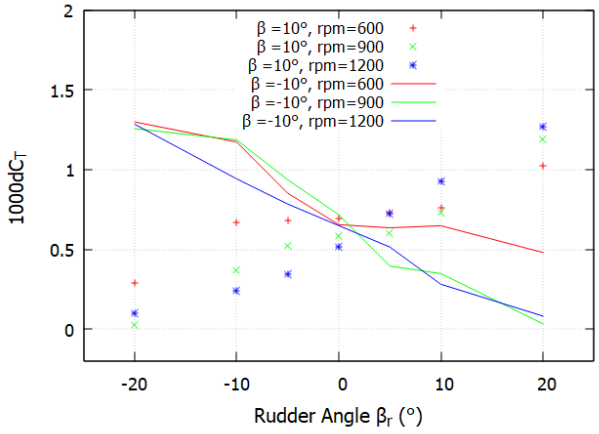

Figure 11: Effect of leeway on total resistance augments, predicted by BEMt, under different RPMs

Table 4: Total drag coefficient at leeway angles +10°and -10°, predicted by Yamazaki under different RPMs

Leeway	Rudder	rpm=600	rpm=900	rpm=1200
+10°	-20°	5.563	7.430	9.448
+10°	-10°	4.998	5.987	7.425
+10°	-5°	4.840	5.738	6.871
+10°	0°	4.788	5.647	6.698
+10°	5°	4.868	5.776	6.899
+10°	10°	5.063	6.115	7.272
+10°	20°	6.076	7.875	9.635
-10°	-20°	6.434	8.327	10.208
-10°	-10°	5.348	6.431	7.865
-10°	-5°	4.949	5.769	7.085
-10°	0°	4.717	5.391	6.629
-10°	5°	4.729	5.373	6.492
-10°	10°	4.929	5.637	6.849
-10°	20°	5.522	6.704	8.163

Figures 12 to 15 illustrate how different propeller revolution rates affect rudder performance under both positive and negative leeway angles, as predicted by the BEMt and Yamazaki models. Both models show a high level of consistency in estimating rudder lift across all tested scenarios and rudder drag in most cases. However, they diverge in estimating rudder drag at the largest rudder angles (20°) at 1200 rpm. This difference is attributed to the Yamazaki model's tendency to overestimate propeller forces compared to the BEMt model, leading to higher inflow velocities at the rudder and subsequently increased rudder drag. With a leeway angle of +10°, the disparity in the C_D curves lessens as propeller revolution rates rise, likely due to the propeller's enhanced ability to straighten the flow. The slope of the lift curve C_L shows an upward trend when the rpm is adjusted from 600 to 1200. For -10° leeway, significantly higher rudder drag is observed at negative rudder angles across all propeller revolutions, and the lift curves display a trend similar to the one seen in the +10° leeway. The verification of the effective wake of the propeller alone in leeway using both BEMt and Yamazaki model can be found in Zhang et al. (2024), where limitations of both body force models were also discussed.

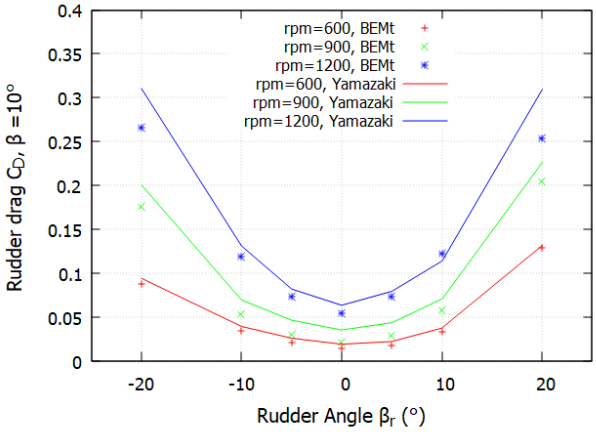

Figure 12: Effect of propeller revolution on rudder drag in +10°leeway

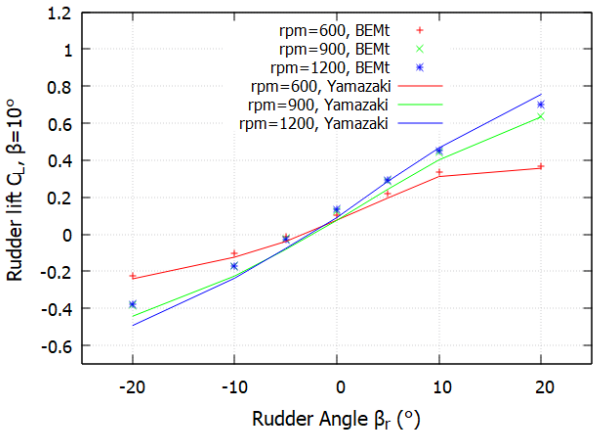

Figure 13: Effect of propeller revolution on rudder lift in +10°leeway

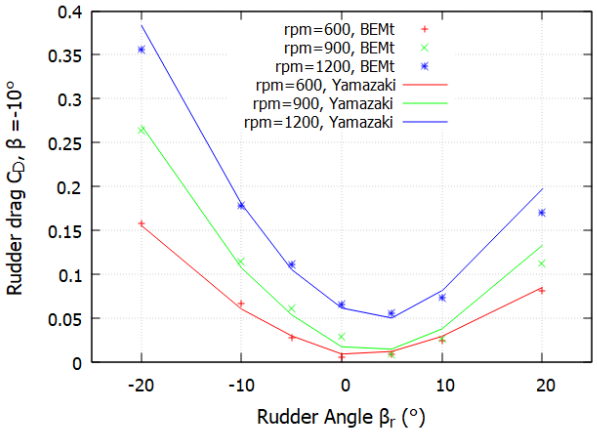

Figure 14: Effect of propeller revolution on rudder drag in -10°leeway

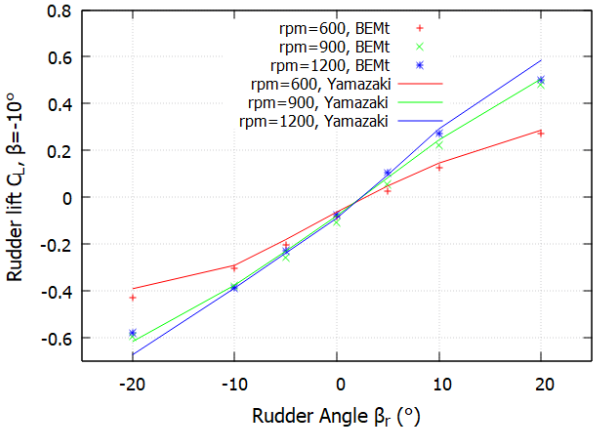

Figure 15: Effect of propeller revolution on rudder lift in -10°leeway

Tables 5 and 6 present the propeller thrust and torque coefficients (dK_T, d10K_Q), calculated based on the difference in propeller forces between leeway conditions (β=-10°, +10°) and a no-leeway scenario (β=0°). It is observed that propeller performance generally degrades more under a +10° leeway angle than at a -10° angle at corresponding rudder angles. This could be attributed to the likelihood

that positive leeway angles promote increased flow separation and turbulence around the propeller, adversely affecting thrust and torque. Furthermore, operating the propeller at a positive leeway angle might lead to unfavourable flow interactions with the rudder positioned downstream, resulting in a more pronounced reduction in propeller efficiency.

Table 5: Propeller thrust augments dK_T at non-zero leeway angles predicted by BEMt

Leeway	Rudder	rpm=600	rpm=900	rpm=1200
+10°	-20°	-0.008	-0.002	-0.005
+10°	-10°	-0.002	-0.002	-0.005
+10°	-5°	-0.002	-0.001	-0.005
+10°	0°	-0.002	0.000	-0.005
+10°	+5°	-0.003	-0.001	-0.004
+10°	+10°	-0.004	-0.001	-0.004
+10°	+20°	0.006	-0.001	-0.005
-10°	-20°	-0.002	-0.005	-0.001
-10°	-10°	0.001	-0.005	-0.002
-10°	-5°	-0.002	-0.005	-0.002
-10°	0°	-0.003	-0.005	-0.002
-10°	+5°	-0.003	-0.006	-0.002
-10°	+10°	-0.002	-0.007	-0.003
-10°	+20°	-0.005	-0.009	-0.003

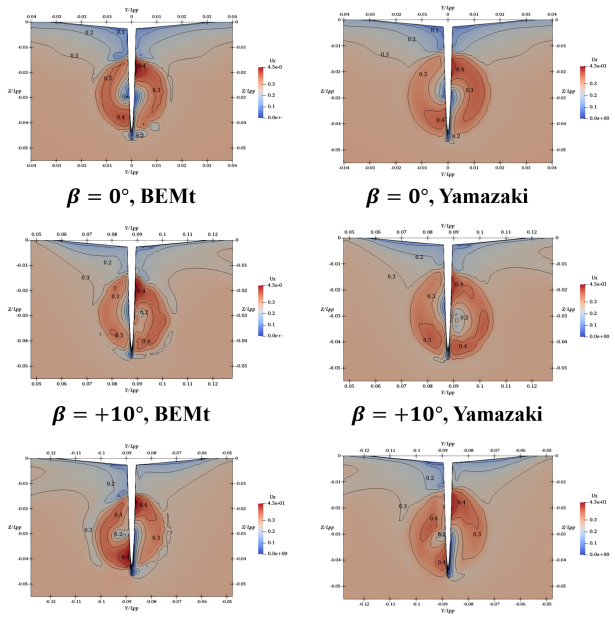

Figure 16: Influence of leeway angle on local velocity profiles at x/Lpp=0.4911, β_r=0°, rpm=600, predicted by BEMt and Yamazaki models.

Figure 16 shows the axial velocity contours at cross-section x/Lpp=0.4911 in three leeways with rpm=600, β_r=0°, predicted by BEMt and Yamazaki model. It is found that the contour's patterns and values show good similarity between both body force models, indicating they can accurately capture the influence of leeway on local axial velocity.

Thrust deduction and wake fraction are two important parameters used to measure the hull-propeller and hull-wake interactions, as defined in Equation 3, in which R_{tow} is the resistance during the resistance test, R_{prop} is the resistance during the fixed RPM test, n is the rotation rate, the equivalent behind-hull advance ration J_i is derived from the open water results. The ratio of thrust deduction and wake fraction is defined as the hull efficiency $\eta_H = \frac{1-t}{1-\omega_t}$. Figures 17-19 present the hull efficiency for three leeway scenarios with different RPMs.

Table 6: Propeller propeller augments $10dK_Q$ at non-zero leeway angles predicted by BEMt

Leeway	Rudder	rpm=600	rpm=900	rpm=1200
+10°	-20°	-0.015	-0.018	-0.011
+10°	-10°	-0.002	-0.014	-0.011
+10°	-5°	-0.003	-0.013	-0.012
+10°	0°	-0.003	-0.012	-0.011
+10°	5°	-0.005	-0.013	-0.009
+10°	10°	-0.007	-0.013	-0.010
+10°	20°	0.010	-0.009	-0.013
-10°	-20°	-0.006	-0.014	-0.004
-10°	-10°	0.001	-0.009	-0.003
-10°	-5°	-0.002	-0.009	-0.006
-10°	0°	-0.004	-0.008	-0.005
-10°	5°	-0.003	-0.012	-0.006
-10°	10°	0.000	-0.011	-0.008
-10°	20°	-0.004	-0.017	-0.011

$$1-t = \frac{T + R_{\text{tow}} - R_{\text{prop}}}{T}, 1-\omega_t = \frac{V_{\text{prop}}}{V_{\text{ship}}} = \frac{J_i D_p n}{V_{\text{ship}}} \quad (3)$$

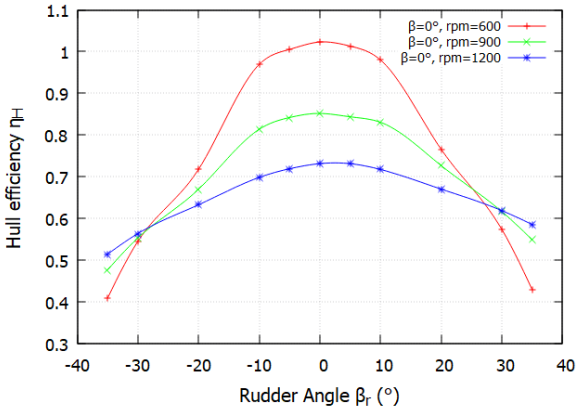

Figure 17: Hull efficiency at 0°leeway.

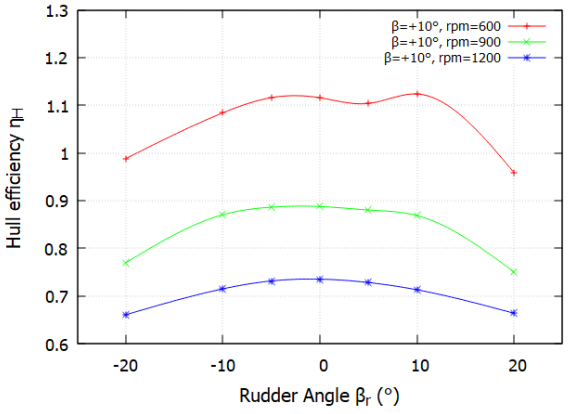

Figure 18: Hull efficiency at +10°leeway.

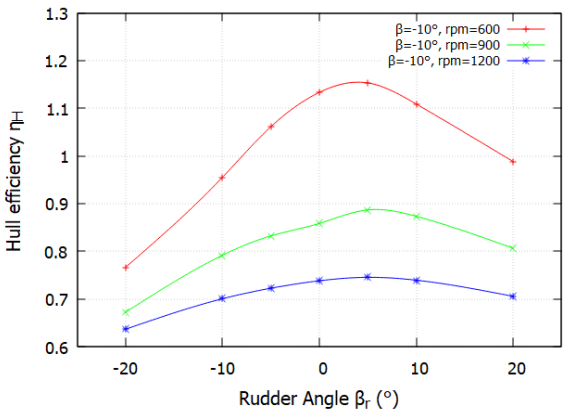

Figure 19: Hull efficiency at $-10°$leeway.

It is found that the variation of rudder angles has a more obvious influence on the hull efficiency at the straight-ahead condition compared to yawed conditions. Both non-zero leeway and higher propeller loading weaken this effect, especially at the positive leeway angle. The applied leeway angle can also affect the rudder angle position at optimal hull efficiency: 0°rudder angle for zero and positive leeway cases while +5°rudder angle for negative leeway scenarios.

6 CONCLUSION

This study investigates the influence of leeway on hull-propeller-rudder interaction using a CFD approach. The fully appended KCS under three different leeway angles combined with a series of rudder angles are simulated in calm water with free surface modelling. Two different body force models are adopted to mimic the propeller action. When the non-zero leeway angle is applied, the drag and lateral force experienced by the hull increase with the increasing rudder angle magnitude. The rotating propeller tends to intensify this increasing trend. The rudder forces are mainly dependent on the upstream propeller and higher propeller loading tends to shift the rudder lift. The effect of leeway on hull efficiency is also presented. Overall, this study contributes to a better understanding of hydrodynamics knowledge of wind-assisted vessels and aids in the optimization of ship designs that harness wind assistance, thereby contributing to maritime decarbonization.

ACKNOWLEDGEMENT

This work is funded by Winds of Change project of Innovate UK. The authors acknowledge the use of the IRIDIS High Performance Computing Facility, and associated support services at the University of Southampton, in the completion of this work.

REFERENCES

Burrill, L.C. (1944). 'Calculation of Marine Propeller Performance Characteristics'. The North East Coast Institution of Engineers and Shipbuilders, Institution Transactions, Volume 60. Bolbec Hall, Newcastle upon Tyne, UK.

ITTC (2014). 'ITTC–Recommended Procedures and Guidelines-Practical Guidelines for Ship CFD

Moriyama, F. (1979). 'On an Approximate Numerical Method for Estimating the Performance of Marine Propellers'. Papers of Ship Research Institute, **16**(6), pp. 361–376.

Meyer, P., Sahab, A., Shevchuk, I., & Abdel-Maksoud, M. (2022). 'Numerical Investigation of the JBC Hull and Propeller Interaction Under Static Drift Condition'. In 34th Symposium on Naval Hydrodynamics, SNH 2022.

Molland, A.F., Turnock, S.R., & Hudson, D.A. (2017). Ship Resistance and Propulsion. Cambridge University Press.

Phillips, A.B., Turnock, S.R., & Furlong, M. (2009). 'Evaluation of manoeuvring coefficients of a self-propelled ship using a blade element momentum propeller model coupled to a Reynolds averaged Navier Stokes flow solver'. Ocean Engineering, **36**(15-16), pp. 1217–1225.

Sanada, Y., Park, S., Kim, D.H., Wang, Z., Stern, F., & Yasukawa, H. (2021). 'Experimental and Computational Study of Hull–Propeller–Rudder Interaction for Steady Turning Circles'. Physics of Fluids, **33**(12).

Larsson, L., Stern, F., & Visonneau, M. (eds.) (2013). Numerical Ship Hydrodynamics: An Assessment of the Gothenburg 2010 Workshop. Springer Science & Business Media.

Hino, T., Stern, F., Larsson, L., Visonneau, M., Hirata, N., & Kim, J. (eds.) (2020). Numerical Ship Hydrodynamics: An Assessment of the Tokyo 2015 Workshop, Vol. 94. Springer Nature.

Turnock, S.R., Phillips, A.B., & Furlong, M. (2008). 'URANS Simulations of Static Drift and Dynamic Manoeuvres of the KVLCC2 Tanker'.

Windén, B. (2021b). 'Predicting the Powering Performance of Different Vessel Types Using an Open-Source CFD Propulsion Framework'. In SNAME Maritime Convention (p. D021S004R004). SNAME.

Winden, B. (2021a). 'An Open-Source Framework for Ship Performance CFD'. In SNAME Offshore Symposium (p. D021S003R002). SNAME.

Yamazaki, R. (1998). 'Deduction of the Simplified Propeller Theory'. Transactions-West Japan Society of Naval Architects, pp. 251–272.

Yamazaki, R. (1968). 'On the Propulsion Theory of Ships on Still Water-Introduction'. Memoirs of the Faculty of Engineering, Kyushu University, **27**(4).

Zhang, Y. (2023). Influence of Drift Angle on the Self-Propelled Ship's Powering Performance in Waves [Doctoral dissertation, University of Southampton].

Zhang, Y., Windén, B., Ojeda, H.R.D., Hudson, D., & Turnock, S. (2024). 'Influence of drift angle on the propulsive efficiency of a fully appended container ship (KCS) using Computational Fluid Dynamics'. Ocean Engineering, **292**, p.116537.